



## Oceanic eddies induce a rapid formation of an internal wave continuum

Luwei Yang <sup>1,3,4</sup>✉, Roy Barkan <sup>1,2</sup>✉, Kaushik Srinivasan<sup>1</sup>, James C. McWilliams<sup>1</sup>, Callum J. Shakespeare<sup>3,4</sup> & Angus H. Gibson<sup>3</sup>

Oceanic internal waves are a major driver for turbulent mixing in the ocean, which controls the global overturning circulation and the oceanic heat and carbon transport. Internal waves are observed to have a continuous energy distribution across all wave frequencies and scales, commonly known as the internal wave continuum, despite being forced at near-inertial and tidal frequencies at large scales. This internal wave continuum is widely thought to be developed primarily through wave-wave interactions. Here we show, using realistic numerical simulations in the subpolar North Atlantic, that oceanic eddies rapidly distribute large-scale wind-forced near-inertial wave energy across spatio-temporal scales, thereby forming an internal wave continuum within three weeks. As a result, wave energy dissipation patterns are controlled by eddies and are substantially enhanced below the mixed layer. The efficiency of this process potentially explains why a phase lag between high-frequency and near-inertial wave energy was observed in eddy-poor regions but not in eddy-rich regions. Our findings highlight the importance of eddies in forming an internal wave continuum and in controlling upper ocean mixing patterns.

<sup>1</sup>Department of Atmospheric and Oceanic Sciences, University of California, Los Angeles, Los Angeles, CA, USA. <sup>2</sup>Porter School of the Environment and Earth Sciences, Tel Aviv University, Tel Aviv, Israel. <sup>3</sup>Research School of Earth Sciences, Australian National University, Canberra, ACT, Australia. <sup>4</sup>ARC Centre of Excellence in Climate Extremes, Australian National University, Canberra, ACT, Australia. ✉email: [luweiy@atmos.ucla.edu](mailto:luweiy@atmos.ucla.edu); [rbarkan@tauex.tau.ac.il](mailto:rbarkan@tauex.tau.ac.il)

Oceanic internal waves are predominantly forced at large horizontal scales; at near-inertial frequencies by time-varying winds, and at the diurnal and semi-diurnal frequencies by barotropic tides<sup>1,2</sup>. However, the measured internal wave field occupies a continuous range of spatio-temporal scales and its energy is distributed across these scales such that the associated energy spectrum falls off gradually from the largest, slowest scales to the smallest, fastest scales<sup>3,4</sup>. Because of this smooth transition across scales, the energy spectrum of the internal wave field is often referred to as the internal wave continuum spectrum, and is modeled empirically by the Garrett-Munk (GM) spectrum<sup>5,6</sup>. The mechanisms that lead to the formation and maintenance of the broad-band continuum spectrum from such narrow-band forcing are crucial to explain how internal waves transfer their energy to small scales where they can break, dissipate energy, and enhance turbulent mixing in the ocean. The corresponding mixing patterns power the global overturning circulation and determine the storage and transport of heat and dissolved gases, and are therefore of utmost importance to the climate system<sup>2,7,8</sup>.

The development of an internal wave continuum has traditionally been attributed to wave-wave interactions that transfer energy from the limited forced scales to a wide range of internal wave scales<sup>9–17</sup>. Recent theoretical and idealized numerical studies suggest that the interactions between ocean eddies and the internal wave field can potentially contribute to the formation of the internal wave continuum spectrum through direct energy transfer from eddies to internal waves<sup>18–22</sup> and through the redistribution of internal wave energy across scales by eddies<sup>19,23–28</sup>. By assuming weak and slowly evolving background flow and linear internal waves with relatively small spatial scales (i.e., the WKB approximation), Kafiabad et al. (2019)<sup>24</sup> showed that a prescribed three-dimensional, homogeneous, and stationary eddy field acted as a diffusion operator, leading to the diffusion of internal wave action across wavenumbers, but along surfaces of constant frequency. Idealized numerical simulations revealed that this wavenumber diffusion mechanism can lead to the formation of an internal wave wavenumber spectrum in tens of days with the same slope as the commonly observed GM wavenumber spectrum<sup>24</sup>. Savva et al. (2021)<sup>26</sup> relaxed the WKB approximation to show that wavenumber diffusion can be explained by a scattering process whereby a stationary geostrophic mode catalyzes the energy transfer between two internal wave modes with slightly different frequencies. Dong et al. (2020)<sup>25</sup> extended these earlier theories and showed that, under the WKB approximation, if the prescribed eddy field was allowed to vary in time it can act as a diffusion operator across frequencies as well. Dong et al. (2023)<sup>28</sup> further demonstrated that over longer time scales the weak background flow assumption of Kafiabad et al. (2019)<sup>24</sup> can break down and that refraction can be important for the scattering of wave energy in frequency space. Because some of the assumptions in these theories do not necessarily hold in the ocean, it remains to be evaluated if and how these eddy-wave interactions contribute to the formation of the commonly observed oceanic internal wave continuum.

Recent ship-based measurements in the Iceland Basin demonstrated that ocean eddies can reduce the horizontal length scales of wind-forced internal waves and modify their propagation<sup>29</sup>. Furthermore, it has been inferred from Argo floats that the energy levels of the eddy field are strongly correlated with regions of enhanced wind-forced internal wave energy dissipation and mixing in the upper ocean<sup>30–32</sup>. However, it remains unclear to what extent eddies distribute wind-forced internal wave energy across spatial and temporal scales and if these distributions contribute to the formation of an internal wave continuum, as suggested by the

earlier theories. Our goal is to assess the role of the eddy field in distributing wave energy to smaller spatio-temporal scales, thereby forming an internal wave continuum, and in controlling the corresponding internal wave dissipation patterns.

To this end, we carry out three sets of high-resolution numerical simulations in the North Atlantic Subpolar Gyre region (Fig. 1a), an area with a rich eddy field that is located along the path of the winter storm tracks<sup>33</sup>. The first set (the eddy-wave case) is a hybrid idealized-realistic computational paradigm that simulates a realistically forced oceanic eddy field and a wind-forced internal wave field generated by a single idealized wind event characteristic of a winter storm in the study region. The realistically-forced eddy field has been previously shown to match well with observations<sup>22</sup>. The second set (the eddy-only case) simulates only the eddy field as in the first set, and the third set (the wave-only case) simulates only the wave field. Each of these three sets of simulations was computed at two different horizontal resolutions, the first at a mesoscale eddy-resolving 2 km horizontal grid spacing, and the second at a submesoscale eddy-resolving 500 m horizontal grid spacing<sup>34</sup>; this choice explicitly allows us to evaluate the role of submesoscale currents in the formation of the internal wave continuum (further details on the numerical simulations are provided in the Methods and Supplementary Note 1). By systematically comparing across the three solution sets we will show that ocean eddies regulate the distribution of wind-forced internal wave energy across spatio-temporal scales, control the formation of an internal wave continuum, and regulate the corresponding dissipation patterns.

## Results

**Simulated eddy and internal wave fields.** The simulated eddy field is illustrated in the eddy-wave case by cyclonic, anticyclonic, and elongated features (associated with oceanic submesoscale fronts and filaments) with strong vorticity on the order of  $f$ , with  $f$  denoting the local Coriolis frequency (Fig. 1b). These features are absent in the wave-only case, resulting in a vorticity field that is two orders of magnitude weaker compared with the eddy-wave case (Fig. 1c).

The resonant response in the oceanic mixed layer following the storm is dominated by inertial oscillations, visualized as circular Lagrangian trajectories that are uniformly distributed across the entire domain in the wave-only case (Supplementary Fig. 3b). The presence of the background eddy field leads to substantially more chaotic Lagrangian trajectories in the eddy-wave case (Supplementary Fig. 3a) than in the wave-only case (Supplementary Fig. 3b).

Initially, the storm injects energy primarily at the inertial frequency (Fig. 2a, and Supplementary Fig. 1), with a domain-averaged near-inertial wind work of  $36.3 \text{ mW m}^{-2}$  and  $42.8 \text{ mW m}^{-2}$  for the eddy-wave case and wave-only case, respectively. The near-inertial wind work in our simulations is representative of the values obtained from observational data in the regions with strong near-inertial energy flux from winds<sup>31</sup>. Immediately after the storm, near-inertial kinetic energy is largely concentrated in the mixed layer (the depth range where the stratification is nearly vertically uniform; Fig. 2b) and then rapidly propagates downward across the base of the mixed layer (the depth where the stratification begins to increase), reaching 800 m depth within a week (Fig. 2c). A complete near-inertial energy budget in the solution sets, including exchanges with lower and higher frequency motions, is deferred to a forthcoming publication.

Accompanying this deep penetration of internal wave energy are elevated magnitudes of internal wave energy dissipation (computed as the super-inertial energy dissipation in an Eulerian reference frame; Methods), characterized by a downward-

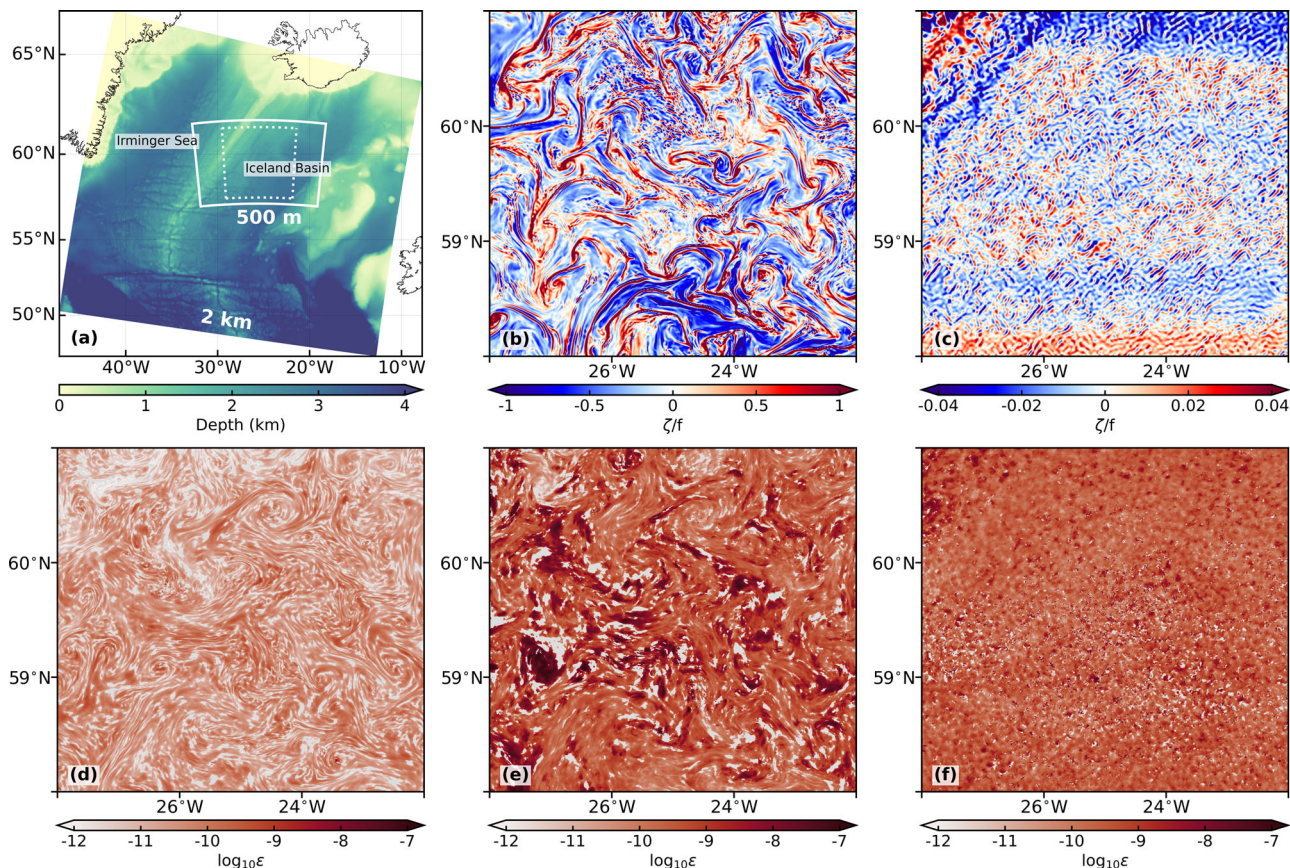


**Fig. 1 Model grids, snapshots of normalized vorticity and super-inertial energy dissipation.** **a** The simulations with 2 km and 500 m resolution are carried out in the colored region and the region in the white box, respectively. The analyses for the 2 km and 500 m simulations are performed in the white dotted box. Colors indicate ocean depth. A snapshot (1 day after the storm) of normalized vorticity at 33 m depth in the **(b)** eddy-wave and **(c)** wave-only cases with 500 m resolution, respectively. Note the different colorbar ranges. The mesoscale cyclonic and anticyclonic eddies are indicated by red and blue circular patterns, respectively, in **(b)**. A snapshot (8 days after the storm) of super-inertial energy dissipation (log scale) at 355 m depth in the **(d)** eddy-only, **(e)** eddy-wave, and **(f)** wave-only cases with 500 m resolution, respectively. Gray colors in **(d-f)** indicate weak negative dissipation values that result from under-sampling of parameterized viscosity values (See Methods and Supplementary Note 7).

propagating signal that extends much deeper in the eddy-wave case than in the wave-only case (Fig. 2e, f). The depth integrated (over the upper 800 m) super-inertial dissipation accounts for 82% and 84% of the near-inertial wind work in the eddy-wave and wave-only cases, respectively, with domain-averaged values of  $3.6 \times 10^{-8} \text{ W kg}^{-1}$  and  $4.4 \times 10^{-8} \text{ W kg}^{-1}$ . However, the energy dissipation averaged between 400 m and 800 m in the eddy-wave case ( $1.7 \times 10^{-9} \text{ W kg}^{-1}$ ) is one order of magnitude larger than that in the wave-only case ( $1.4 \times 10^{-10} \text{ W kg}^{-1}$ ). In the eddy-only case there is little internal wave energy dissipation below the mixed layer (Fig. 2d), with a domain average of  $2.2 \times 10^{-10} \text{ W kg}^{-1}$ , 2–3 orders of magnitude smaller than the corresponding values in the eddy-wave and wave-only cases.

In addition to the differences in vertical extent, the lateral distributions of internal wave energy dissipation below the mixed layer are strongly affected by the eddy field. In contrast with the horizontally homogeneous distribution of internal wave energy dissipation in the wave-only case (Fig. 1f), the corresponding dissipation patterns in the eddy-wave case are much more spatially variable (Fig. 1e), illustrating the important role the eddy field plays in modulating internal wave energy dissipation patterns.

**Internal wave energy distribution across temporal scales.** The frequency spectra of kinetic energy for all the simulations at 33 m and 355 m depths are shown to assess the impact of the eddy field

on the distribution of internal wave energy across temporal scales (Fig. 3). These depths represent locations within and beneath the mixed layer, respectively.

In the eddy-only case (dotted black line in Fig. 3) the frequency spectrum is energetic in the sub-inertial frequency range, corresponding to the eddy field, and falls off rapidly in the super-inertial frequency range due to the absence of wave forcing. The inertial peak is substantially reduced but still noticeable, because the daily filtering operation of the wind stress is imperfect. In the wave-only case (dashed black line in Fig. 3) the energy levels are substantially reduced in the sub-inertial frequency range, as expected, and a sharp inertial peak is evident. Additional energetic peaks appear at the inertial super-harmonics, with low energy levels in the troughs in between. The formation mechanism of the super-harmonics is not investigated further here, but it has been previously reported in the literature<sup>35–39</sup>. The lack of continuity in the energy spectrum in this case suggests that wave-wave interactions are insufficient to distribute internal wave energy across all the time scales simulated here. In the eddy-wave case, however, an internal wave continuum spectrum in the super-inertial frequency range develops, especially in the 500 m simulations.

The comparison of frequency spectra between the eddy-wave and wave-only cases (solid black and dashed lines in Fig. 3) indicates that the eddy field plays an important role in distributing internal wave energy to fill up the energy gaps

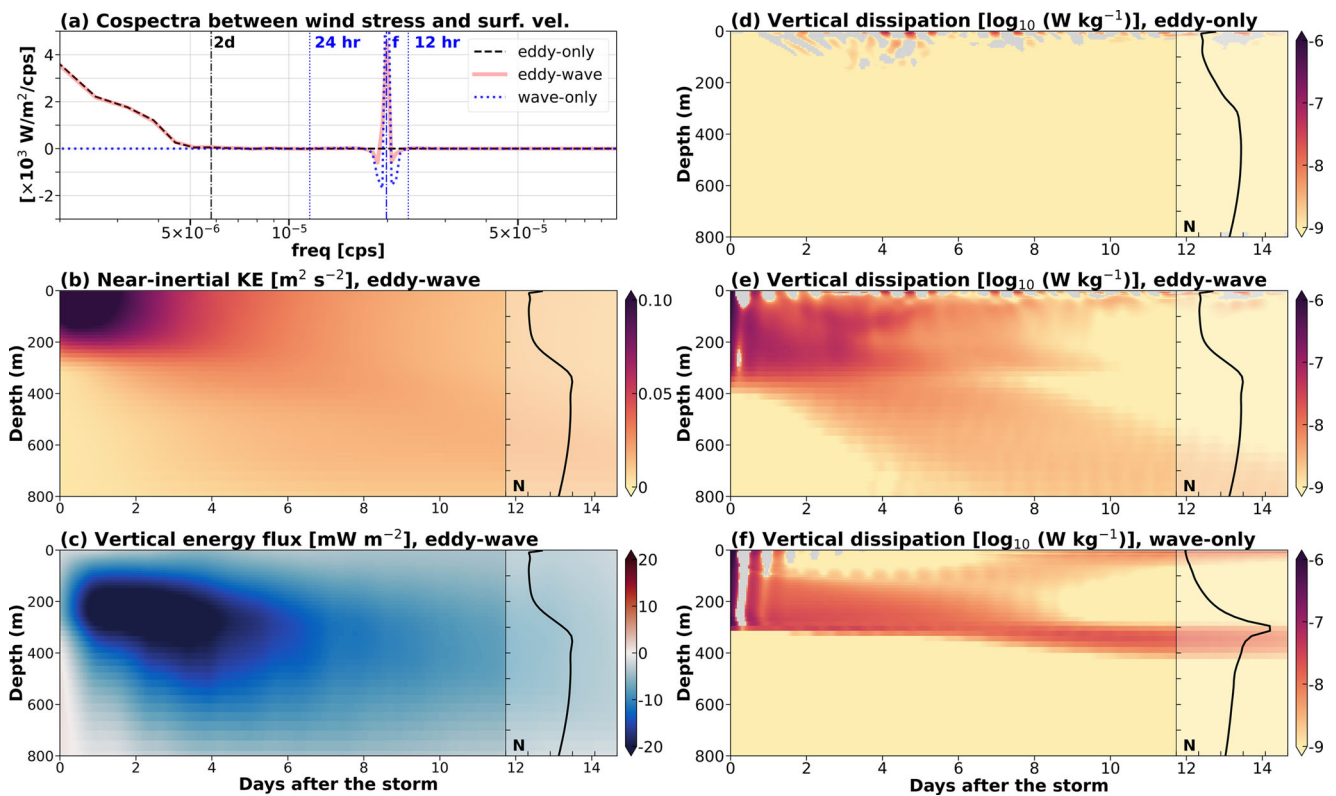


**Fig. 2** The generation, propagation, and dissipation of near-inertial kinetic energy. **a** The wind work cospetrum in the eddy-only, eddy-wave, and wave-only cases. The frequency band over which the near-inertial wind work, near-inertial kinetic energy, and near-inertial vertical energy flux are computed is defined between 12 h and 24 h, which are marked by blue dotted lines. The Hövmoller diagram of **(b)** near-inertial kinetic energy and **(c)** vertical energy flux in the eddy-wave case, respectively. The negative vertical energy flux indicates downward energy propagation. The Hövmoller diagram of horizontally averaged super-inertial energy dissipation (log scale) in the **(d)** eddy-only, **(e)** eddy-wave, and **(f)** wave-only cases, respectively (Methods). As in Fig. 1, gray colors in **(d-f)** indicate weak negative dissipation values that result from under-sampling of parameterized viscosity values (Methods and Supplementary Note 7). Solid lines in **(b-f)** show the horizontally and temporally averaged stratification profiles with an x-axis ranges from 0 to  $0.005 \text{ s}^{-1}$ . The quantities shown are obtained from the 2 km simulations. See Supplementary Fig. 4 for the same figure for the 500 m simulations.

shown in the wave-only case, resulting in a developed internal wave continuum spectrum with a spectral slope close to the commonly observed GM slope of  $-2^3-6$ . Furthermore, the overall spectral shape is consistent with the observed spectra in the study region<sup>22,40</sup> and many other locations in the ocean<sup>41</sup>. The improvements in the internal wave continuum spectrum at the 500 m simulations may potentially be explained by a non-negligible contribution by submesoscale currents<sup>42</sup>, which are only resolved at this resolution.

To evaluate the contribution of Doppler shifting by lower-frequency currents (like eddies) to the observed distribution of internal wave energy across a wide range of time scales<sup>43,44</sup>, we compute the frequency spectrum in the eddy-wave case on Lagrangian particles (Methods). Comparing between the resulting Lagrangian frequency spectrum and the Eulerian frequency spectrum (solid red and black lines in Fig. 3) is a natural way to identify Doppler shifting effects<sup>45,46</sup>. The most prominent differences between the Eulerian and Lagrangian spectra are seen near the surface in the sub-inertial frequency range for the 500 m simulation (solid black and red curves in Fig. 3c). The elevated sub-inertial energy levels in the Lagrangian spectra indicates a return of sub-inertial energy to lower frequencies in the Lagrangian reference frame; the shift of this part of energy to higher sub-inertial frequencies in the Eulerian reference frame may potentially be explained by the sweeping of sub-inertial submesoscale currents by the mean flow past an Eulerian observer, as discussed in ref. <sup>47</sup>. Most importantly, little differences are found between the Eulerian and Lagrangian

spectra in the super-inertial frequency range at all depths and across the two resolutions. This indicates that in this region the distribution of wind-forced internal wave energy across time scales cannot be solely attributed to Doppler shifting effects.

**Internal wave energy distribution across spatial scales.** To examine the impact of the eddy field on the distribution of internal wave energy across spatial scales at each frequency band, we show the frequency-horizontal-wavenumber spectra of internal wave energy in the 500 m solutions for the eddy-wave and wave-only cases at 33 m and 355 m depths (Fig. 4). Here, the internal wave energy is the super-inertial kinetic energy computed in the Lagrangian reference frame (i.e., with horizontal Doppler shifting removed).

The comparison between the frequency-wavenumber spectra at the two depths (Fig. 4c, g) shows much larger energy values in the eddy-wave case across a wide range of frequencies, especially in the frequency bands bounded by inertial super-harmonics, consistent with Fig. 3. In the wave-only case, the internal wave energy is distributed in narrow frequency bands centered around inertial frequency and its super-harmonics (i.e.,  $f$ ,  $2f$ ,  $3f$ ); along these frequency bands, the internal wave energy is distributed across a wide range of length scales, from the domain scale to the smallest scale resolved in the simulations (Fig. 4). In the eddy-wave case, the internal wave energy in the frequency ranges bounded by inertial frequency and its super-harmonics also spreads over a wide range of length scales. The corresponding

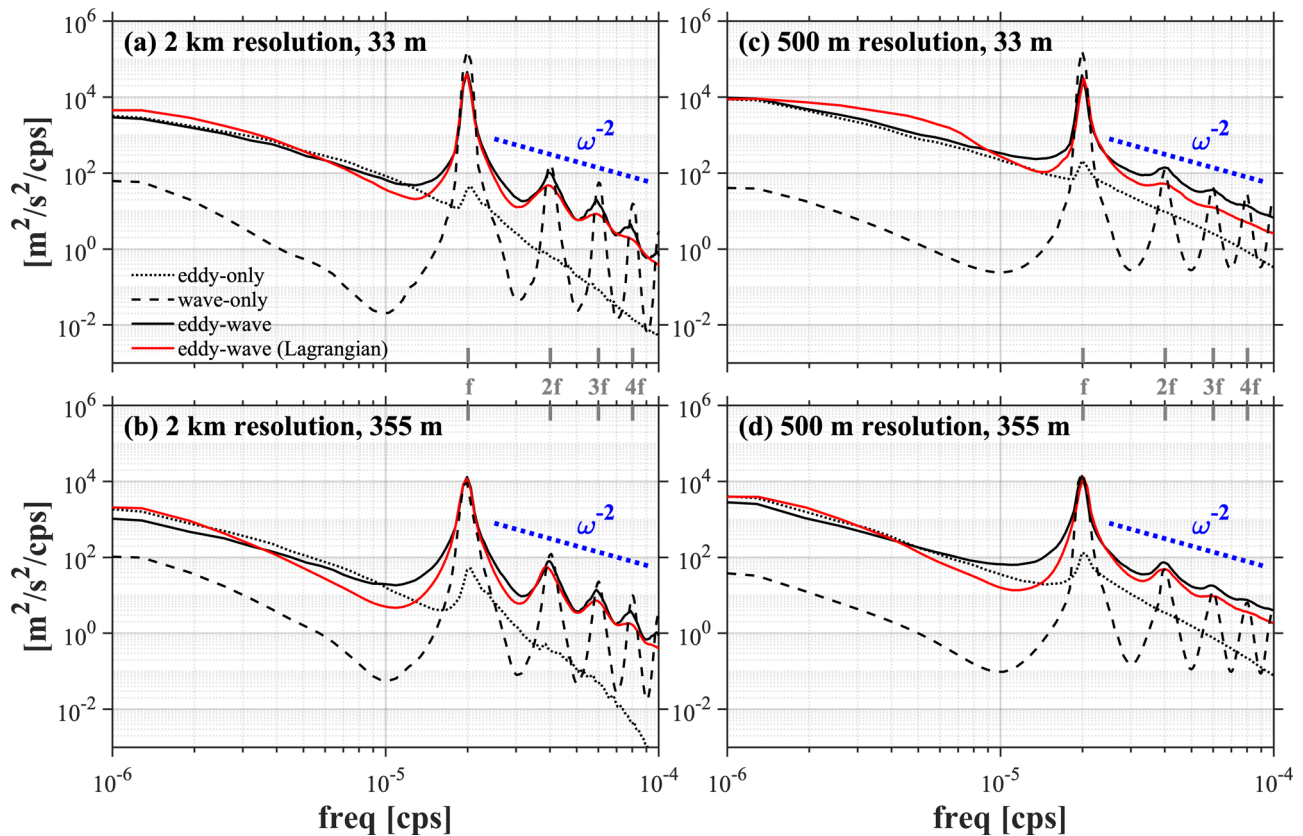


**Fig. 3 Kinetic energy distribution in frequency space.** Frequency spectra of kinetic energy in the eddy-only (dotted lines), eddy-wave (solid lines), and wave-only (dashed lines) cases for the (a) 2 km simulations at 33 m depth, (b) 2 km simulations at 355 m depth, (c) 500 m simulations at 33 m depth, and (d) 500 m simulations at 355 m depth. The red curves indicate the Lagrangian spectrum (Supplementary Note 6) in the eddy-wave case. A slope of -2 representing the shape of GM spectrum is marked in blue dotted lines for comparison.

horizontal wavenumber spectra show that the presence of the eddy field leads to the filling up of energy at smaller scales, at the expense of larger scales, with an increased effect below the mixed layer at 355 m depth (Fig. 4d, h). The spectral slopes at both depths in the eddy-wave case are much closer to the commonly observed GM spectral slope (dotted blue line in Fig. 4d, h). Similar qualitative results are found in the 2 km solutions (Supplementary Fig. 5), although, quantitatively the differences are larger in magnitude in the finer 500 m solutions.

**Internal wave energy dissipation.** To evaluate how the differences in spatial patterns of internal wave energy dissipation (Figs. 1d–f, 2d–f) are related to the spatio-temporal distribution of internal wave energy (Figs. 3, 4), we compute the frequency-horizontal-wavenumber cospectrum of kinetic energy dissipation below the mixed layer, at 355 m depth (Fig. 5; Methods). The internal wave energy dissipation in the model is dominated by the vertical mixing component<sup>48</sup> that is designed to parameterize internal wave breaking and vertical shear instability.

Consistent with Figs. 1d and 2d, the internal wave energy dissipation in the eddy-only case is 2–3 orders of magnitude smaller than that in the eddy-wave and wave-only cases (Fig. 5a, d). In the wave-only case, the internal wave energy dissipation is limited to narrow bands around the inertial frequency and its super-harmonics (Fig. 5c, f). At these frequency bands, the internal wave energy dissipation occurs over a wide range of horizontal wavenumbers and is dominated by 10–100 km scales (Fig. 5c, f). In the eddy-wave case, however, the internal wave energy dissipation occurs across a wide range of internal wave frequencies (Fig. 5b, e), presumably as a result of

the spreading of wave energy by eddies across frequencies (Fig. 3). In the frequency bands bounded by inertial frequency and its harmonics, the internal wave energy dissipation is observed down to the smallest horizontal length scales that are adequately resolved in the simulations (dashed vertical lines in Fig. 5), presumably as a result of the spreading of wave energy by eddies across horizontal wavenumbers (Fig. 4d, h).

## Discussion

The above numerical results and analyses demonstrate that oceanic mesoscale eddies and submesoscale currents can play a crucial role in the formation of the internal wave energy continuum (i.e., the GM spectrum) and in the associated spatio-temporal distributions and spatial patterns of internal wave dissipation. Specifically, we demonstrate that in the submesoscale-permitting 2 km resolution eddy-wave model, the simulated continuum is not perfectly smooth and marked by spectral peaks at higher inertial harmonics, i.e.,  $2f$ ,  $3f$ , and  $4f$ . In the 500 m submesoscale-resolving eddy-wave model, however, we observe a pronounced decrease in the amplitude of these peaks and a more realistic internal wave continuum<sup>22</sup>, highlighting the importance of interactions between smaller, faster submesoscales and internal waves in accurately simulating the continuum.

We further show that eddy-wave interactions lead to the emergence of a continuum spectrum within 3 weeks following a storm; in the absence of eddies, no such continuum is formed. The efficiency of this mechanism is key to explaining why observations find that the seasonal cycle of high-frequency wave energy is in phase with that of near-inertial wave energy in regions of high eddy energy, but lags that of near-inertial energy

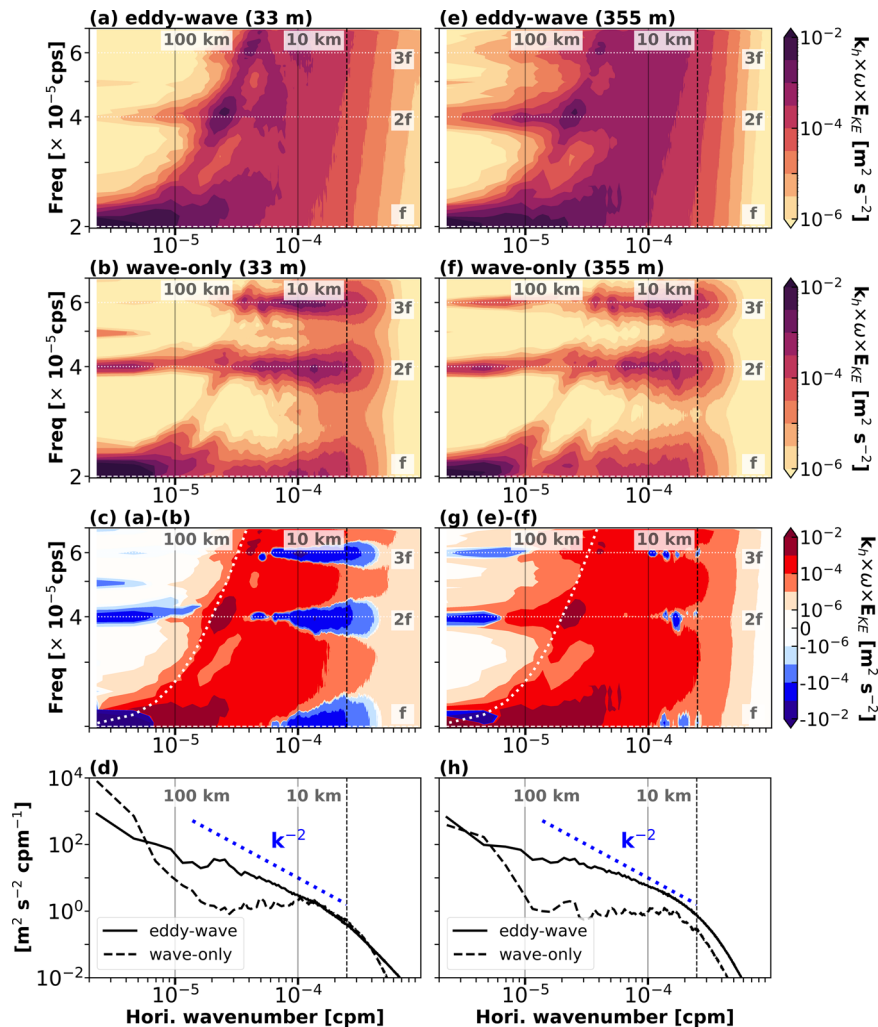


**Fig. 4 Internal wave energy distribution in frequency-horizontal-wavenumber space.** Frequency-horizontal-wavenumber spectrum of internal wave energy at (a–b) 33 m depth and (e–f) 355 m depth from 500 m simulations in the eddy-wave and wave-only cases, respectively. The internal wave energy is computed using super-inertial high-pass velocities on Lagrangian particles with a temporal resolution of 2 h (Nyquist frequency of  $7.0 \times 10^{-5} \text{ s}^{-1}$ ; see Methods). The corresponding differences in the energy spectrum between the eddy-wave and wave-only cases at (c) 33 m depth and (g) 355 m depth. The associated horizontal wavenumber spectra of internal wave energy in the eddy-wave (solid lines) and wave-only (dashed lines) cases at (d) 33 m depth and (h) 355 m depth. The white horizontal lines in (a–c) and (e–g) mark  $f$ ,  $2f$ , and  $3f$  (where  $f$  is the inertial frequency), respectively. The white dotted curves in (c) and (g) mark the dispersion relation for mode-1 baroclinic internal waves (Supplementary Note 5). Dashed, black vertical lines mark the horizontal wavenumber corresponding to eight grid spacings. At higher wavenumbers, horizontal numerical diffusion is important (note the spectral roll-off) and the modeled dynamics can no longer be considered inviscid. See Supplementary Figure 5 for the same figure for 2 km simulations.

in regions of low eddy energy<sup>3</sup>. We also demonstrate that oceanic eddies play a crucial role in regulating internal wave energy dissipation patterns, leading to substantial enhancements below the mixed layer in the thermocline region.

Our results can be related to recent theoretical studies suggesting that the spreading of wave energy in wavenumber space results from the advection by a weak background flow (i.e., wavenumber diffusion)<sup>24,26,27</sup>, whereas the spreading of wave energy in frequency space results from the advection by a (weak) time-dependent background flow (i.e., frequency diffusion)<sup>25</sup> or, alternatively, from refraction over a longer time scale when the weak flow assumption breaks down<sup>28</sup>. However, whether the physical mechanisms responsible for the eddy-induced effects in our simulations can be attributed to these theories is unclear, because the underlying weak refraction approximation<sup>24–26</sup> and spatial scale separation assumption<sup>28</sup> do not hold in the numerical simulations presented here. For example, although the time scale for the formation of an internal wave wavenumber

continuum in our simulation is consistent with that suggested by ref.<sup>24</sup> (tens of days), we also obtain an internal wave frequency continuum over the same time scale; much more rapidly than predicted by the refraction mechanism<sup>28</sup>.

In this study internal tides are intentionally eliminated to focus on the interaction between eddies and wind-forced internal waves, which are believed to be a major driver of turbulent mixing in the upper ocean<sup>2,41</sup>. In the time scale considered here, wave-wave interactions produce super-harmonics across a wide range of wavenumbers but are not sufficient to form an internal wave continuum in both frequency and wavenumber space. It is evident that wave-wave interactions are expected to increase when internal tides are also forced<sup>3,49,50</sup>, and that they can independently lead to the formation of a GM-like spectrum<sup>14,49,51–53</sup>. The dominant mechanisms at play may thus vary regionally and depend on the relative magnitudes of the near-inertial waves, the internal tides, and the eddy field. We note in passing, that in upcoming work we find that in eddy rich

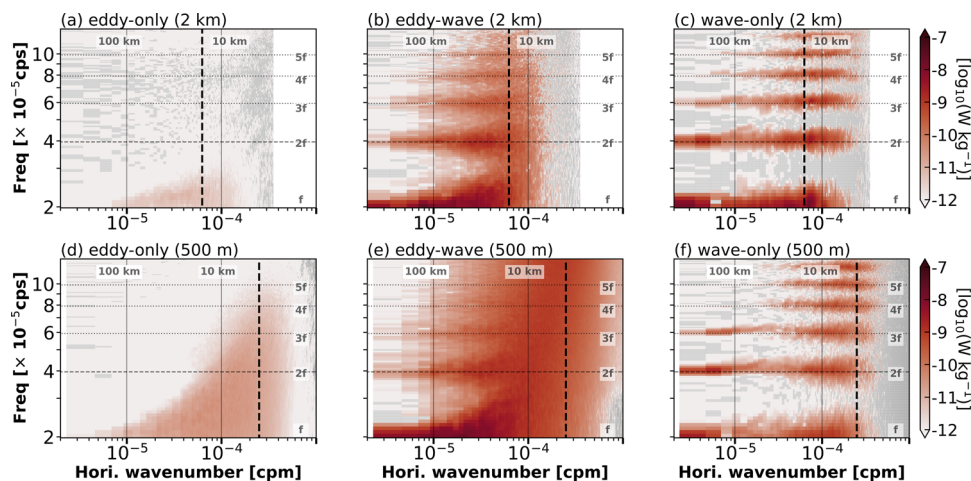


**Fig. 5** The internal wave energy dissipation in frequency-horizontal wavenumber space. The energy dissipation cospectrum (log scale) in the frequency-horizontal-wavenumber space at 355 m depth for (a–c) 2 km simulations and (d–f) 500 m simulations in the eddy-only, eddy-wave, and wave-only cases, respectively. The energy dissipation cospectrum is computed using hourly Eulerian velocity and vertical viscosity fields (Nyquist frequency of  $\approx 1.4 \times 10^{-4} \text{ s}^{-1}$ ; see Methods) and only the super-inertial part of the cospectrum is shown. Dashed, black vertical lines mark the horizontal wavenumber corresponding to eight grid spacings, after which horizontal numerical diffusion is significant. Gray colors indicate weak negative dissipation values that result from under-sampling of parameterized viscosity values (Methods and Supplementary Note 7). The mean and standard deviation of these negative values in (a–f) are  $-(2.5 \pm 3.4) \times 10^{-14}$ ,  $-(3.4 \pm 4.1) \times 10^{-12}$ ,  $-(4.3 \pm 4.9) \times 10^{-12}$ ,  $-(4.9 \pm 6.4) \times 10^{-14}$ ,  $-(5.1 \pm 8.8) \times 10^{-13}$ ,  $-(2.8 \pm 3.6) \times 10^{-12}$ , respectively.

regions corresponding to the north Atlantic and the California Current System, scattering of waves by eddies is found to be far more important than wave-wave interactions.

As part of our analysis, we demonstrate that horizontal Doppler shifting of wave frequency by currents plays a negligible role in distributing wind-forced internal wave energy across time scales. Although, it may be more important in regions with strong currents like those found in western boundary currents and the Southern Ocean<sup>46,54</sup>. We emphasize that we only consider the effect of horizontal Doppler shifting because the Lagrangian spectra are obtained from advecting particles using the horizontal velocity. We acknowledge that the high wavenumber/frequency part of the continuum spectrum may be contaminated by vertical Doppler shifting<sup>43,55,56</sup>, especially in the 500 m resolution simulations where the frontal vertical circulations are present<sup>57</sup>. Addressing the effects of vertical Doppler shifting through particle advection in three dimensions will be the subject of future studies.

Our results imply that turbulent mixing in the upper ocean, which is associated with the breaking of wind-forced internal waves, is likely to be sensitive to climate change because both atmospheric wind forcing<sup>58</sup> and the oceanic eddy field are expected to vary in the future<sup>59</sup>. However, current representation of turbulent mixing in climate models relies on numerical parameterizations that do not account for this sensitivity<sup>60</sup>. The physical processes described here need to be incorporated into the parameterizations to better simulate and predict its impacts on key climate processes, such as the vertical heat transport and the uptake of anthropogenic carbon in a changing climate.

## Methods

**Numerical simulations.** The high-resolution numerical simulations of the North Atlantic subpolar gyre region are carried out using Coastal and Regional Ocean COMMunity model (CROCO; <http://www.croco-ocean.org/>). All three sets of simulations are performed at 2 km and 500 m resolution and are analyzed for 18 days following the idealized wind event. The 500 m simulations are nested down from the 2 km simulations<sup>61</sup>. The model solution in the domain of 500 m simulations (indicated by a

white dotted box in Fig. 1a) is analyzed in the 2 km simulations for comparison with the 500 m simulations.

The eddy-only case is forced by the daily realistic low-passed wind stress and initialized with an eddy field. The daily low-passed wind stress (Supplementary Fig. 1) is produced by a simulation forced by daily low-passed wind velocity from the NCEP Climate Forecast System Reanalysis<sup>62</sup> with hourly temporal resolution<sup>22</sup>. The eddy field used as the initial and boundary conditions is taken from the smooth forcing simulation in ref. <sup>22</sup> that has been validated against the AVISO dataset, Argo and mooring-based measurements collected in the study region. Other forcing and boundary conditions used in the eddy-only case are identical to the smooth forcing simulation in ref. <sup>22</sup>. The eddy-only case is designed to ensure that the flow field consists of realistic mesoscale and submesoscale eddies but is absent of internal waves.

The eddy-wave case is forced by the same low frequency wind stress as the eddy-only case, with an isolated resonant wind stress superimposed to generate an idealized atmospheric storm event (Supplementary Fig. 1). The resonant wind stress lasts effectively for one inertial period and has the magnitude of  $2 \text{ N m}^{-2}$ , which is characteristic of observed winter storms in the North Atlantic subpolar gyre region<sup>63</sup>. The eddy-wave case uses the same boundary and initial conditions as in the eddy-only case. The eddy-wave case represents a realistic scenario following an isolated winter storm where internal waves are generated and propagate into a realistic mesoscale and submesoscale eddy field.

The wave-only case is forced only by the resonant wind stress to exclude the generation of the eddy field by low frequency wind stress. The initial velocity field and the velocity at the four side boundaries are all set to zero to simulate a quiescent ocean absent of eddies. The temperature and salinity profiles used as initial and boundary conditions are obtained by horizontally averaging the initial temperature and salinity fields in the eddy-wave case and are kept horizontally constant to prevent the generation of geostrophic currents due to horizontal density variations. The resulting stratification profile is well within the stratification distribution of the eddy-wave solution (Supplementary Fig. 2).

Note that the simulations are designed to artificially exclude locally and remotely generated internal tides; wind-forced internal waves are the only internal wave source in the simulations. Further details on the simulation setup are provided in Supplementary Note 1.

**Energy dissipation.** In CROCO, the vertical mixing of momentum and tracers is computed using a  $K$ -profile parameterization<sup>48</sup>; the horizontal mixing is computed using a third-order, upstream biased advection scheme that contains an implicit horizontal hyperdiffusion<sup>64</sup>. In the ocean interior, outside of the boundary layers, the  $K$ -profile parameterization is designed to parameterize shear instability, internal wave breaking, and double diffusion<sup>48</sup> by instantaneously increasing the mixing coefficient for momentum and tracers, i.e., viscosity ( $\nu_v$ ) and diffusivity ( $\kappa_v$ ). The corresponding numerical energy dissipation comprises vertical mixing and horizontal diffusion<sup>65</sup>, and is dominated by its vertical component in our simulations. This vertical dissipation takes the form

$$D = \tau \frac{\partial \mathbf{u}}{\partial z}, \quad (1)$$

in units of  $\text{W kg}^{-1}$ , where the viscous stress  $\tau$  is computed using the parameterized viscosity and vertical shear following

$$\tau = \nu_v \frac{\partial \mathbf{u}}{\partial z}. \quad (2)$$

The super-inertial energy dissipation shown in Figs. 1, 2 is computed using the coarse-graining approach<sup>66</sup> with a fourth order low-passed Butterworth filter,

$$D = \overline{\tau \frac{\partial \mathbf{u}}{\partial z}} - \overline{\tau} \frac{\partial \overline{\mathbf{u}}}{\partial z}, \quad (3)$$

where  $\overline{(\ )}$  indicates the low-passed field and the cutoff period is the domain-averaged inertial period of 14 h. Note that  $\nu_v$  may vary on shorter time scales than the hourly model output frequency used here, because the parameterization is designed to act instantaneously from one time step to another. This sampling bias can lead to erroneous negative dissipation values, which are masked in Figs. 1, 2.

**Spectral analyses.** The wind work cospectrum shown in Fig. 2a is computed using the 18-day surface velocity and wind stress time series and is interpreted as the wind energy input across frequencies. The frequency spectrum of kinetic energy in the Eulerian frame shown in Fig. 3 is computed using the 18-day velocity time series ( $\mathbf{u}(t)$  at each grid point) counting from the beginning of the simulations. The time series at each grid point at the selected depth is first demeaned and detrended, then Hann windowed (the energy loss due to the windowing is compensated), and finally discrete Fourier transformed to compute the wind work cospectrum and frequency spectrum. The final spectrum and cospectrum are obtained by averaging over all grid points in the analysis region.

The Lagrangian frequency spectrum of kinetic energy is computed in the same way as the Eulerian frequency spectrum, except that Lagrangian velocity time series of the same period are used. The Lagrangian velocity time series are constructed by advecting particles from grid points forward and backward in time with a 9-day time window<sup>45</sup>; the advection is initialized from the twelfth hour in day 9 to ensure that the backward advection covers the first half of the Eulerian time series, and the forward advection the second.

Note that the Lagrangian velocity time series come with a caveat: Lagrangian particles are only allowed to move horizontally and they sample velocities unevenly over the domain due to horizontal divergence or convergence of the flow. The divergent

region repels Lagrangian particles and is therefore under-sampled. The convergent region attracts and accumulates Lagrangian particles and may therefore be over-represented in the final spectrum. The total energy of the Lagrangian spectrum is theoretically equal to that of the Eulerian spectrum (i.e., the conservation of energy) because the Doppler shift effect redistributes energy in the frequency space without adding or removing energy. However, this divergence/convergence-induced bias in sampling will change the energy content of the Lagrangian spectrum, especially in the 500 m simulation near the surface where the submesoscale currents and their associated strong vertical velocity are better simulated. Indeed, the total energy of Lagrangian spectrum is slightly smaller than that of the Eulerian spectrum in the 2 km simulation but larger in the 500 m simulation. Compared with the total energy of Eulerian spectrum, the total energy of Lagrangian spectrum decreases by 7% and 5% at 33 m depth and 355 m depth, respectively, in the 2 km simulation; in contrast, the total energy of Lagrangian spectrum increases by 13% and 3% at 33 m depth and 355 m depth, respectively, in the 500 m simulation. To address this sampling bias, we normalize the Lagrangian spectrum to ensure that its energy content matches that of the Eulerian spectrum.

The frequency-horizontal-wavenumber spectrum of internal wave energy shown in Fig. 4 is computed using the super-inertial Lagrangian velocity time series. For a given snapshot, the super-inertial Lagrangian velocity at a grid point is obtained by high-passing a 6-day Lagrangian time series using a fourth order Butterworth filter with a cutoff frequency of  $1.98 \times 10^{-5}$  cps; the 6-day Lagrangian time series consists of two 3-day segments, the first and second 3-day segment are obtained by advecting particles backward and forward in time from this grid point, respectively, following ref. <sup>45</sup>. The window size used for forward and backward advection is selected based on a detailed sensitivity test (Supplementary Note 6). This analysis is repeated for every other snapshot (i.e., every other hour) ranging from 84 h to 394 h after the beginning of the simulations. The length of high-passed Lagrangian velocity time series is 310 h and the temporal resolution is 2 h. The frequency-horizontal-wavenumber spectrum is calculated following the same steps as calculating the frequency spectrum, except that the horizontal Lagrangian velocity field  $\mathbf{u}^L(x, y, t)$  is directly used. The frequency-horizontal-wavenumber spectra in Fig. 4 have been multiplied by frequency  $\omega$  and horizontal wavenumber  $k_h$  to preserve their variance in log-log space.

The advection window size used in the Lagrangian filtering (3-day) and for constructing the Lagrangian spectrum (9-day) are different because the Lagrangian time series are constructed for different purposes. In the Lagrangian filtering, the 6-day Lagrangian time series are constructed to obtain the Lagrangian velocity field. It is the time series of the Lagrangian velocity field not the 6-day Lagrangian time series that are used to compute the frequency-horizontal-wavenumber spectrum of internal wave energy. In addition, computing Lagrangian velocity is computationally expensive because the two-way advection is repeated for all grid points ( $287 \times 287$  for the 2 km simulations and  $866 \times 866$  for the 500 m simulations) at all 156 snapshots for each depth. Therefore, the advection window size (3-day) is chosen based on the minimum length of time series segments that retain the internal wave energy in the original time series (Supplementary Note 6). In contrast, the 18-day Lagrangian time series are constructed to compute the Lagrangian frequency spectrum for a direct comparison with the Eulerian frequency spectrum. Therefore, the advection window size has to be half of the length of Eulerian time series (9-day). This 9-day advection is carried out only once (at the middle snapshot of the 18-day time series) for all grid points.



**Kinetic energy dissipation cospectrum.** Below we derive the kinetic energy dissipation in spectral space, focusing for brevity on the zonal momentum equation

$$\hat{u}_t + \dots = \hat{\tau}_z, \quad (4)$$

where the hat operator denotes a Fourier transform in time and space, subscripts denote derivatives, ... denote all other terms, and the parametrized stress  $\tau$  is given in Eq. (2). Next, we multiply Eq. (4) by the complex conjugate  $\hat{u}^*$  and add it to  $\hat{u}$  multiplied by the complex conjugate of Eq. (4) to obtain

$$\hat{u}^* \hat{u}_t + \hat{u} \hat{u}_t^* + \dots = \hat{u}^* \hat{\tau}_z + \hat{u} \hat{\tau}_z^*, \quad (5)$$

$$\Rightarrow \frac{\partial |\hat{u}|^2}{\partial t} + \dots = \partial_z (\hat{u}^* \hat{\tau} + \hat{u} \hat{\tau}^*) - (\hat{u}_z^* \hat{\tau} + \hat{u}_z \hat{\tau}^*), \quad (6)$$

making use of the chain rule.

The energy dissipation cospectrum shown in Fig. 5 is computed using the real part of the cross-spectral density of vertical shear and viscous stress (last term in Eq. 6). The dissipation cospectrum measures the correlation between vertical shear and viscous stress in spectral space. High cospectral density corresponds to strong energy dissipation. The dissipation cospectra shown in Fig. 5 are also multiplied by frequency  $\omega$  and horizontal wavenumber  $k_h$  to preserve variance in log-log space. As discussed in the Methods section, the under-sampling of  $v_v$  results in negative cospectrum values, which are masked in Fig. 5. When the  $v_v$  field is smoothed these negative values disappear (see Supplementary Fig. 8 for illustration).

#### Data availability

The processed data that support the figures in this study are archived at <https://doi.org/10.5281/zenodo.8063764>. The NCEP Climate Forecast System Reanalysis products used to force the simulations are available at <https://rda.ucar.edu/datasets/ds093-2/>.

#### Code availability

The CROCO code is publicly available at <https://www.croco-ocean.org/>. The input files that are used to set up the simulations and the code used to process data and plot figures are available upon request to L.Y. or R.B.

Received: 6 June 2023; Accepted: 21 November 2023;

Published online: 16 December 2023

#### References

- Garrett, C. & Kunze, E. Internal tide generation in the deep ocean. *Annu. Rev. Fluid Mech.* **39**, 57–87 (2007).
- Alford, M. H., Mackinnon, J. A., Simmons, H. L. & Nash, J. D. Near-inertial internal gravity waves in the ocean. *Ann. Rev. Mari. Sci.* **8**, 95–123 (2016).
- Polzin, K. L. & Lvov, Y. V. Toward regional characterizations of the oceanic internal wavefield. *Rev. Geophys.* **49**, 329 (2011).
- Le Boyer, A. & Alford, M. H. Variability and sources of the internal wave continuum examined from global moored velocity records. *J. Phys. Oceanogr.* **51**, 2807–2823 (2021).
- Garrett, C. & Munk, W. Space-time scales of internal waves. *Geophys. Fluid Dyn.* **3**, 225–264 (1972).
- Garrett, C. & Munk, W. Space-time scales of internal waves: A progress report. *J. Geophys. Res.* **80**, 291–297 (1975).
- MacKinnon, J. A. et al. Climate process team on internal wave-driven ocean mixing. *Bull. Am. Meteorol. Soc.* **98**, 2429–2454 (2017).
- Whalen, C. B. et al. Internal wave-driven mixing: governing processes and consequences for climate. *Nat. Rev. Earth. Environ.* **1**, 606–621 (2020).
- Olbers, D. J. Nonlinear energy transfer and the energy balance of the internal wave field in the deep ocean. *J. Fluid Mech.* **74**, 375–399 (1976).
- McComas, C. H. & Bretherton, F. P. Resonant interaction of oceanic internal waves. *J. Geophys. Res.* **82**, 1397–1412 (1977).
- Pomphrey, N., Meiss, J. D. & Watson, K. M. Description of nonlinear internal wave interactions using Langevin methods. *J. Geophys. Res. Oceans* **85**, 1085–1094 (1980).
- McComas, C. H. & Müller, P. The dynamic balance of internal waves. *J. Phys. Oceanogr.* **11**, 970–986 (1981).
- Müller, P., Holloway, G., Henyey, F. & Pomphrey, N. Nonlinear interactions among internal gravity waves. *Rev. Geophys.* **24**, 493–536 (1986).
- Hibiya, T., Nagasawa, M. & Niwa, Y. Nonlinear energy transfer within the oceanic internal wave spectrum at mid and high latitudes. *J. Geophys. Res. Oceans* **107**, 21–28 (2002).
- Polzin, K. Idealized solutions for the energy balance of the finescale internal wave field. *J. Phys. Oceanogr.* **34**, 231–246 (2004).
- Lvov, Y. V., Polzin, K. L. & Yokoyama, N. Resonant and near-resonant internal wave interactions. *J. Phys. Oceanogr.* **42**, 669–691 (2012).
- Eden, C., Pollmann, F. & Olbers, D. Numerical evaluation of energy transfers in internal gravity wave spectra of the ocean. *J. Phys. Oceanogr.* **49**, 737–749 (2019).
- Taylor, S. & Straub, D. Forced near-inertial motion and dissipation of low-frequency kinetic energy in a wind-driven channel flow. *J. Phys. Oceanogr.* **46**, 79–93 (2016).
- Barkan, R., Winters, K. B. & McWilliams, J. C. Stimulated imbalance and the enhancement of eddy kinetic energy dissipation by internal waves. *J. Phys. Oceanogr.* **47**, 181–198 (2017).
- Rocha, C. B., Wagner, G. L. & Young, W. R. Stimulated generation: Extraction of energy from balanced flow by near-inertial waves. *Journal of Fluid Mechanics* **847**, 417–451 (2018).
- Taylor, S. & Straub, D. Effects of adding forced near-inertial motion to a wind-driven channel flow. *J. Phys. Oceanogr.* **50**, 2983–2996 (2020).
- Barkan, R. et al. Oceanic mesoscale eddy depletion catalyzed by internal waves. *Geophys. Res. Lett.* **48**, e2021GL094376 (2021).
- Savva, M. A. C. & Vanneste, J. Scattering of internal tides by barotropic quasigeostrophic flows. *J. Fluid Mech.* **856**, 504–530 (2018).
- Kafiabad, H. A., Savva, M. A. C. & Vanneste, J. Diffusion of inertia-gravity waves by geostrophic turbulence. *J. Fluid Mech.* **869**, R7 (2019).
- Dong, W., Bühler, O. & Smith, K. S. Frequency diffusion of waves by unsteady flows. *J. Fluid Mech.* **905**, R3 (2020).
- Savva, M. A. C., Kafiabad, H. A. & Vanneste, J. Inertia-gravity-wave scattering by three-dimensional geostrophic turbulence. *J. Fluid Mech.* **916**, A6 (2021).
- Cox, M. R., Kafiabad, H. A. & Vanneste, J. Inertia-gravity-wave diffusion by geostrophic turbulence: the impact of flow time dependence. *J. Fluid Mech.* **958**, A21 (2023).
- Dong, W., Bühler, O. & Smith, K. S. Geostrophic Eddies Spread Near-Inertial Wave Energy to High Frequencies. *J. Phys. Oceanogr.* **53**, 1311–1322 (2023).
- Thomas, L. N. et al. Direct Observations of Near-Inertial Wave  $\zeta$ -Refraction in a Dipole Vortex. *Geophys. Res. Lett.* **47**, e2020GL090375 (2020).
- Whalen, C. B., Talley, L. D. & MacKinnon, J. A. Spatial and temporal variability of global ocean mixing inferred from Argo profiles. *Geophys. Res. Lett.* **39**, L18612 (2012).
- Whalen, C. B., MacKinnon, J. A. & Talley, L. D. Large-scale impacts of the mesoscale environment on mixing from wind-driven internal waves. *Nat. Geosci.* **11**, 842–847 (2018).
- Liu, Z. & Liao, G. Relationship between global ocean mixing and coherent mesoscale eddies. *Deep Sea Res. Part I: Oceanogr. Res. Pap.* **197**, 104067 (2023).
- Hoskins, B. J. & Hodges, K. I. New perspectives on the Northern Hemisphere winter storm tracks. *J. Atmos. Sci.* **59**, 1041–1061 (2002).
- Srinivasan, K., Barkan, R. & McWilliams, J. C. A forward energy flux at submesoscales driven by frontogenesis. *J. Phys. Oceanogr.* **53**, 287–305 (2023).
- Niwa, Y. & Hibiya, T. Nonlinear processes of energy transfer from traveling hurricanes to the deep ocean internal wave field. *J. Geophys. Res. Oceans* **102**, 12469–12477 (1997).
- Danioux, E. & Klein, P. A resonance mechanism leading to wind-forced motions with a  $2f$  frequency. *J. Phys. Oceanogr.* **38**, 2322–2329 (2008).
- Komori, N., Ohfuchi, W., Taguchi, B., Sasaki, H. & Klein, P. Deep ocean inertia-gravity waves simulated in a high-resolution global coupled atmosphere-ocean GCM. *Geophys. Res. Lett.* **35**, L04610 (2008).
- Danioux, E. et al. Emergence of wind-driven near-inertial waves in the deep ocean triggered by small-scale eddy vorticity structures. *J. Phys. Oceanogr.* **41**, 1297–1307 (2011).
- Wagner, G. L. & Young, W. R. A three-component model for the coupled evolution of near-inertial waves, quasi-geostrophic flow, and the near-inertial second harmonic. *J. Fluid Mech.* **802**, 806–837 (2016).
- Vic, C., Ferron, B., Thierry, V., Mercier, H. & Lherminier, P. Tidal and near-inertial internal waves over the Reykjanes Ridge. *J. Phys. Oceanogr.* **51**, 419–437 (2021).
- Ferrari, R. & Wunsch, C. Ocean circulation kinetic energy: reservoirs, sources, and sinks. *Ann. Rev. Fluid Mech.* **41**, 253–282 (2009).
- McWilliams, J. C. Submesoscale currents in the ocean. *Proc. R. Soc. A: Math. Phys. Eng. Sci.* **472**, 20160117 (2016).
- Pinkel, R. Advection, phase distortion, and the frequency spectrum of finescale fields in the sea. *J. Phys. Oceanogr.* **38**, 291–313 (2008).
- Pinkel, R. Vortical and internal wave shear and strain. *J. Phys. Oceanogr.* **44**, 2070–2092 (2014).

45. Shakespeare, C. J. et al. A new open source implementation of lagrangian filtering: a method to identify internal waves in high-resolution simulations. *J. Adv. Model. Earth Syst.* **13**, e2021MS002616 (2021).
46. Rama, J., Shakespeare, C. J. & Hogg, A. M. Importance of background vorticity effect and doppler shift in defining near-inertial internal waves. *Geophys. Res. Lett.* **49**, e2022GL099498 (2022).
47. Callies, J., Barkan, R. & Naveira Garabato, A. C. Time scales of submesoscale flow inferred from a mooring array. *J. Phys. Oceanogr.* **50**, 1065–1086 (2020).
48. Large, W. G., McWilliams, J. C. & Doney, S. C. Oceanic vertical mixing: a review and a model with a nonlocal boundary layer parameterization. *Rev. Geophys.* **32**, 363–403 (1994).
49. Nelson, A. D. et al. Improved internal wave spectral continuum in a regional ocean model. *J. Geophys. Res.: Oceans* **125**, e2019JC015974 (2020).
50. Arbic, B. K. Incorporating tides and internal gravity waves within global ocean general circulation models: a review. *Prog. Oceanogr.* **206**, 102824 (2022).
51. Sugiyama, Y., Niwa, Y. & Hibiya, T. Numerically reproduced internal wave spectra in the deep ocean. *Geophys. Res. Lett.* **36**, L07601 (2009).
52. Chen, Z. et al. Can tidal forcing alone generate a GM-Like internal wave spectrum? *Geophys. Res. Lett.* **46**, 14644–14652 (2019).
53. Peddada, S. H. & Chalamalla, V. K. Numerical simulations of internal gravity wave resonant triads. *Phys. Fluids* **35**, 086609 (2023).
54. Nagai, T., Tandon, A., Kunze, E. & Mahadevan, A. Spontaneous generation of near-inertial waves by the Kuroshio Front. *J. Phys. Oceanogr.* **45**, 2381–2406 (2015).
55. Sherman, J. T. & Pinkel, R. Estimates of the vertical wavenumber-frequency spectra of vertical shear and strain. *J. Phys. Oceanogr.* **21**, 292–303 (1991).
56. Alford, M. H. Fine-structure contamination: observations and a model of a simple two-wave case. *J. Phys. Oceanogr.* **31**, 2645–2649 (2001).
57. Thomas, L. N. Enhanced radiation of near-inertial energy by frontal vertical circulations. *J. Phys. Oceanogr.* **49**, 2407–2421 (2019).
58. Chang, E. K. M. & Yau, A. M. W. Northern Hemisphere winter storm track trends since 1959 derived from multiple reanalysis datasets. *Clim. Dyn.* **47**, 1435–1454 (2016).
59. Martínez-Moreno, J. et al. Global changes in oceanic mesoscale currents over the satellite altimetry record. *Nat. Clim. Change* **11**, 397–403 (2021).
60. Fox-Kemper, B. et al. Challenges and prospects in ocean circulation models. *Front. Mar. Sci.* **6**, 65 (2019).
61. Mason, E. et al. Procedures for offline grid nesting in regional ocean models. *Ocean Model.* **35**, 1–15 (2010).
62. Saha, S. et al. The NCEP climate forecast system reanalysis. *Bull. Am. Meteorol. Soc.* **91**, 1015–1058 (2010).
63. Pineau-Guillou, L. et al. Strong winds in a coupled wave-atmosphere model during a North Atlantic storm event: evaluation against observations. *Q. J. R. Meteorol. Soc.* **144**, 317–332 (2018).
64. Lemarié, F. et al. Are there inescapable issues prohibiting the use of terrain-following coordinates in climate models? *Ocean Model.* **42**, 57–79 (2012).
65. Gula, J., Molemaker, M. J. & McWilliams, J. C. Topographic generation of submesoscale centrifugal instability and energy dissipation. *Nat. Commun.* **7**, 12811 (2016).
66. Eyink, G. L. & Aluie, H. Localness of energy cascade in hydrodynamic turbulence. I. Smooth coarse graining. *Phys. Fluids* **21**, 115107 (2009).

## Acknowledgements

L.Y., R.B., K.S., and J.C.M were supported by ONR-N000141812697. RB was also supported by the Israeli Science Foundation grant 1736/18. Resources supporting this work were provided by the NSF XSEDE project OCE030007 and ACCESS project EES220050.

## Author contributions

L.Y., R.B., and K.S. led the design of the experiments. L.Y. performed the numerical simulations and led the analysis of the results, with significant contributions from R.B., K.S., C.J.S., and A.H.G. L.Y. and R.B. led the manuscript writing and interpretation of the results, with significant contributions from K.S., J.C.M., C.J.S., and A.H.G.

## Competing interests

The authors declare no competing interests.

## Additional information

**Supplementary information** The online version contains supplementary material available at <https://doi.org/10.1038/s43247-023-01137-1>.

**Correspondence** and requests for materials should be addressed to Luwei Yang or Roy Barkan.

**Peer review information** *Communications Earth & Environment* thanks the anonymous reviewers for their contribution to the peer review of this work. Primary Handling Editors: Viviane Menezes, Heike Langenberg. A peer review file is available.

**Reprints and permission information** is available at <http://www.nature.com/reprints>

**Publisher's note** Springer Nature remains neutral with regard to jurisdictional claims in published maps and institutional affiliations.



**Open Access** This article is licensed under a Creative Commons Attribution 4.0 International License, which permits use, sharing, adaptation, distribution and reproduction in any medium or format, as long as you give appropriate credit to the original author(s) and the source, provide a link to the Creative Commons license, and indicate if changes were made. The images or other third party material in this article are included in the article's Creative Commons license, unless indicated otherwise in a credit line to the material. If material is not included in the article's Creative Commons license and your intended use is not permitted by statutory regulation or exceeds the permitted use, you will need to obtain permission directly from the copyright holder. To view a copy of this license, visit <http://creativecommons.org/licenses/by/4.0/>.

© The Author(s) 2023